RF system models for the CERN Large Hadron Collider with application to longitudinal dynamics

T. Mastorides,* C. Rivetta,† J. D. Fox, and D. Van Winkle
Stanford Linear Accelerator Center, Stanford, California 94309, USA

P. Baudrenghien
CERN, Geneva, Switzerland

(Received 15 July 2010; published 13 October 2010)

The Large Hadron Collider rf station-beam interaction strongly influences the longitudinal beam dynamics, both single-bunch and collective effects. Nonlinearities and noise generated within the radio frequency (rf) accelerating system interact with the beam and contribute to beam motion and longitudinal emittance blowup. Thus, the noise power spectrum of the rf accelerating voltage strongly affects the longitudinal beam distribution. Furthermore, the coupled-bunch instabilities are also directly affected by the rf components and the configuration of the low level rf (LLRF) feedback loops. In this work we present a formalism relating the longitudinal beam dynamics with the rf system configurations, an estimation of collective effects stability margins, and an evaluation of longitudinal sensitivity to various LLRF parameters and configurations.

DOI: 10.1103/PhysRevSTAB.13.102801 PACS numbers: 29.20.db, 29.27.Bd

I. INTRODUCTION

The Large Hadron Collider (LHC) rf system consists of eight rf stations per beam. The rf system accelerates the beam during the ramp, compensates the small energy losses during coasting, and also provides longitudinal focusing. The beam and the rf station are two dynamic systems with a strong interaction, which complicates stability considerations for the composite system. A simplified block diagram of the LHC rf system is shown in Fig. 1.

Each rf station includes an accelerating superconducting cavity, a 330 kW klystron, and the low level rf (LLRF) system consisting of the klystron polar loop and the impedance control feedback system. The superconducting cavity has an R/Q of 45, a resonance frequency of 400.8 MHz, and a mechanical tuner with a 100 kHz range. The cavity voltage and loaded quality factor Q_L are set to 1 MV and 20 000, respectively, during injection and to 2 MV and 60 000 during physics, for nominal intensity beams. The klystron polar loop used at the LHC acts around the klystron to reject power supply perturbations and compensate the gain and phase shift of the nonlinear klystron at low frequencies for different operation points. The feedback system controls the accelerating fundamental impedance of the rf station to achieve longitudinal stability. It incorporates digital and analog paths, as well as the 1-Turn feedback (comb), which acts to reduce the impedance at the synchrotron sidebands.

Single-bunch longitudinal emittance growth as well as beam stability related to collective effects are examined in this paper. Both of these longitudinal dynamics effects are strongly coupled to the effective impedance of the rf station and the configurations of the feedback loop. The rf configuration is defined by the design choices of components and signal levels, as well as the operational choices of variable parameters. Different approaches on the component and parameter selection can have a significant effect on the stability and characteristics of the beam.

In this work, the LHC LLRF system has been modeled with the existing technology implementation. The effect of the operational choices on controller settings is then investigated. The objective of this work is to verify high-current and upgraded operating conditions of the LHC, study optimal configuration techniques to achieve minimum rf

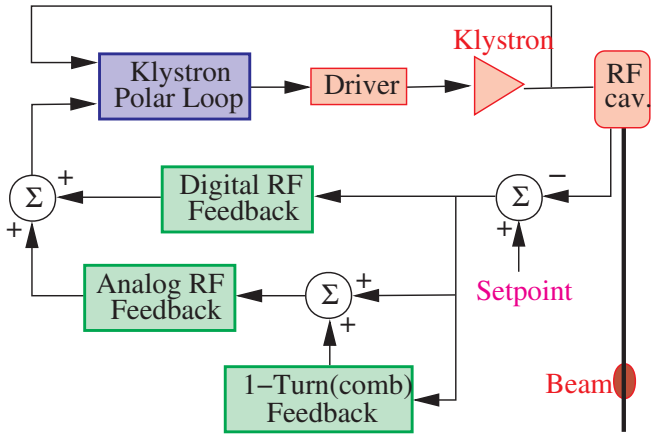

FIG. 1. (Color) Simplified LHC rf block diagram.

*themis@slac.stanford.edu
†rivetta@slac.stanford.edu

station effective impedance, estimate noise and stability limits of the system, and possible impacts of technical aspects of the implementation. An ultimate goal is to use this knowledge to build a base of future impedance-controlled rf and LLRF system techniques for upgrades of existing or future machines.

Section II outlines the major noise sources of the system and defines their relationship with the rf accelerating voltage noise. In Sec. III a quantitative description of the relationship between the noise spectral density and the longitudinal beam emittance will be presented, as a function of the rf loop configuration and the system noise. With this formalism and the simplification from Sec. II, it is then possible to study the single-bunch dynamics for rf configurations of interest, as shown in Sec. IV. The stability criterion for coupled-bunch instabilities, the estimated growth rates, and the sensitivity of collective effects on the rf parameters are discussed in Sec. V.

II. NOISE SOURCES

The single-bunch longitudinal emittance growth greatly depends on the noise level in the rf accelerating voltage. The major noise sources in the rf system include components in the LLRF boards, the rf reference (local oscillator), the klystron driver amplifier, the klystron power supply, low frequency sources (microphonics, ground vibrations, cooling system, etc.), the effect of the nonuniform beam current on the rf cavity voltage, and more. The spectrum of these sources spans from very low to very high frequencies.

The models presented in this paper work for both low frequency and wideband sources. Initial measurements suggest that the LLRF noise contributions are indeed wideband, but that there are also significant contributions from the rf reference (local oscillator) at low frequencies. The quantitative results presented in this paper assume wideband sources for simplicity, in particular the LLRF noise and the klystron driver amplifier, as shown in Fig. 2. The LLRF noise includes several contributions such as the digital quantizing noise and arithmetic noise in digital signal processing, thermal noise, analog/digital demodulator, and modulator. Based on an understanding of the engineering implementation of the system, these sources can be considered broadband and incoherent.

It should be noted that the klystron power supplies introduce coherent noise at the 50 Hz harmonics in all the stations. The synchrotron frequency crosses the 50 Hz line during the ramp, which can lead to a resonant effect [1]. The longitudinal emittance growth formalism presented in this work does not include this phenomenon.

The individual noise sources for the LLRF components are distributed throughout the electronics of the system. To be able to effectively study the various contributions, it is helpful to concentrate them in two equivalent noise sources located either at the input of the LLRF board, or the output

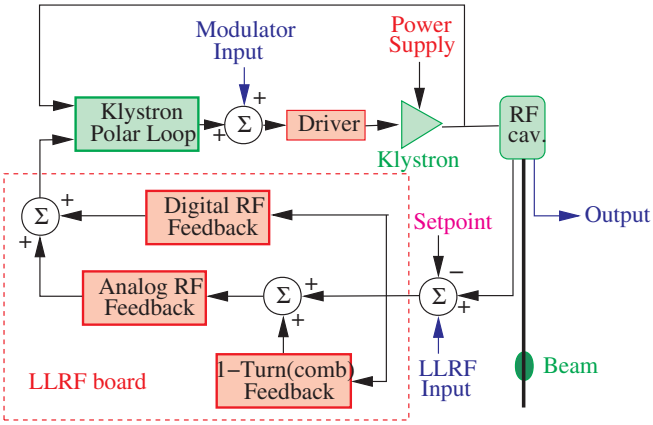

FIG. 2. (Color) Noise sources. Blocks in red represent the major noise sources, in blue are the equivalent noise sources for simulations purposes, and the other components are shown in green.

of the klystron polar loop (the input of the modulator), as shown in Fig. 2. Both of these sources are in baseband and can be modeled as two independent sources in the in-phase (i) and quadrature (q) channels, for a total of four noise sources.

The accelerating voltage noise is modeled in amplitude $a_{\mathrm{cav}}(t)$ and phase $\phi_{\mathrm{cav}}(t)$. To calculate the relationship between an input vector perturbation at the mth source

$$n^m(t) = \begin{pmatrix} n_i^m \\ n_q^m \end{pmatrix}$$

and the amplitude or phase of the cavity voltage, we linearize the response of the rf station around the operation point and determine the impulse response $h^m(t)$ between the output and the input,

$$\begin{pmatrix} a_{\mathrm{cav}}^m(t) \\ \phi_{\mathrm{cav}}^m(t) \end{pmatrix} = \begin{bmatrix} h_{ai}^m & h_{aq}^m \\ h_{\phi i}^m & h_{\phi q}^m \end{bmatrix} * \begin{pmatrix} n_i^m \\ n_q^m \end{pmatrix}(t) = \begin{pmatrix} h_a^m \\ h_\phi^m \end{pmatrix} * n^m(t),$$

where $*$ denotes convolution and $h_a^m = [h_{ai}^m h_{aq}^m]$ and $h_\phi^m = [h_{\phi i}^m h_{\phi q}^m]$.

Since the system is linear, we can use superposition to get

$$\begin{pmatrix} a_{\mathrm{cav}}(t) \\ \phi_{\mathrm{cav}}(t) \end{pmatrix} = \sum_m \begin{pmatrix} h_a^m \\ h_\phi^m \end{pmatrix} * n^m(t), \tag{1}$$

where the summation is over all the noise sources. The impulse responses $h^m(t)$ depend on the operational configuration of the rf station.

III. FORMALISM FOR BUNCH LENGTH ESTIMATION

During a long store, the bunch energy spread and longitudinal emittance shrink due to the small synchrotron radiation damping, whereas any noise injected in the ac-

celerating rf voltage leads to longitudinal emittance blowup. Optimally, these two mechanisms should balance and the beam should keep a constant bunch length. In this section, a formalism relating the bunch emittance growth with the noise in the accelerating voltage is presented. The accelerating voltage depends strongly on the configurations of the rf station and the LLRF feedback systems.

Following [2], it can be shown that the longitudinal equations of beam motion are

$$\begin{aligned}\dot{\phi} &= \frac{\eta\omega_{\mathrm{rf}}}{E_o}\epsilon \\ \dot{\epsilon} &= \frac{1}{T_o}[qV_o\sin(\phi_s+\phi) - U_{\mathrm{rad}}(\epsilon+E_o)],\end{aligned} \tag{2}$$

where ϕ, ϵ are the phase and energy of the particles with respect to the synchronous particle, the rf voltage is $V_{\mathrm{rf}} = V_o\sin(\phi_s+\phi)$, η is the slip factor, E_o the beam energy, T_o the revolution period, q the charge of a proton, ω_{rf} the angular rf frequency, ϕ_s the phase of the synchronous particle, and $U_{\mathrm{rad}}(E)$ the synchrotron radiation energy emitted by a particle of energy E over a turn. It should be noted that even though this equation is defined for a single particle, it extends to the whole multiparticle bunch. This set of equations can be described as a stochastic differential equation.

The cavity amplitude noise $a_{\mathrm{cav}}(t)$ and phase noise $\phi_{\mathrm{cav}}(t)$ are sampled by the beam with a period T_o resulting in the perturbations $a(t)$ and $\tilde{\phi}(t)$. In the presence of these perturbations, the beam motion Eq. (2) becomes

$$\begin{aligned}\dot{\phi} &= \frac{\eta\omega_{\mathrm{rf}}}{E_o}\epsilon \\ \dot{\epsilon} &= \frac{1}{T_o}\{qV_o[1+a(t)]\sin[\phi_s+\phi-\tilde{\phi}(t)] \\ &\quad - U_{\mathrm{rad}}(\epsilon+E_o)\} \\ &= \frac{1}{T_o}(qV_o[1+a(t)]\{\sin(\phi_s)\cos[\phi-\tilde{\phi}(t)] \\ &\quad + \cos(\phi_s)\sin[\phi-\tilde{\phi}(t)]\} - U_{\mathrm{rad}}(\epsilon+E_o)).\end{aligned} \tag{3}$$

For small energy oscillations, ϵ and ϕ are close to zero, so it is possible to linearize around the synchronous particle coordinates. Then, Eq. (3) becomes

$$\begin{aligned}\dot{\epsilon} &= \frac{1}{T_o}(qV_o\{\sin(\phi_s) + [\phi-\tilde{\phi}(t)]\cos(\phi_s) + a(t) \\ &\quad \times \sin(\phi_s)\} - U_o - \epsilon D) \\ &= \frac{1}{T_o}(qV_o\{[\phi-\tilde{\phi}(t)]\cos(\phi_s) + a(t)\sin(\phi_s)\} - \epsilon D),\end{aligned} \tag{4}$$

where $D \approx 2U_o/E_o$ with U_o the synchrotron radiation of the synchronous particle, and $qV_o\sin(\phi_s) = U_o$. The second order perturbation term $a(t)[\phi-\tilde{\phi}(t)]\cos(\phi_s) \approx 0$ has been dropped.

It is obvious from Eq. (4) that the phase noise is much more significant than the amplitude noise, since ϕ_s is close to 180°, so that

$$[\phi-\tilde{\phi}(t)]\cos(\phi_s) \gg a(t)\sin(\phi_s).$$

Therefore, using Eqs. (2) and (4), and assuming that the amplitude noise is negligible, we get the linearized longitudinal equations of motion:

$$\dot{\phi} = \frac{\eta\omega_{\mathrm{rf}}}{E_o}\epsilon \qquad \dot{\epsilon} = \frac{q\dot{V}_{\mathrm{rf}}(0)}{\omega_{\mathrm{rf}}T_o}[\phi-\tilde{\phi}(t)] - \frac{D}{T_o}\epsilon, \tag{5}$$

where $\dot{V}_{\mathrm{rf}}(0) = \omega_{\mathrm{rf}}V_o\cos(\phi_s)$ is the rf gradient for the synchronous particle.

The particle beam samples the cavity phase noise $\phi_{\mathrm{cav}}(t)$ every revolution harmonic, so that

$$\begin{aligned}\tilde{\phi}(t) &= \sum_{k=-\infty}^{\infty}\delta(t-kT_o)\phi_{\mathrm{cav}}(t) \\ &= \sum_{k=-\infty}^{\infty}\delta(t-kT_o)\sum_m h_\phi^m * n^m(t)\end{aligned}$$

according to Eq. (1). To simplify the notation, and since the noise sources are uncorrelated, the analysis is carried using a generic representation for one of the terms in the summation over m, so that

$$\tilde{\phi}(t) = \sum_{k=-\infty}^{\infty}\delta(t-kT_o)(h_g * n_g)(t),$$

where (h_g, n_g) could be either $(h_{\phi i}, n_i)$ or (h_{ϕ_q}, n_q). The approximation of the sampling by an impulse is still valid for the ensemble of equations of all particles in a bunch, since the 1 ns bunch is very fast compared to the period of the loop dynamics (approximately 3 μs, since the bandwidth of ϕ_{cav} is roughly 300 kHz).

To simplify the equations of motion, ϵ is transformed to a normalized momentum p,

$$p = \frac{\eta\omega_{\mathrm{rf}}}{E_o}\epsilon,$$

so that Eq. (5) becomes

$$\dot{\phi} = p \qquad \dot{p} = -\omega_s^2\phi - 2\alpha p + \omega_s^2\tilde{\phi}(t), \tag{6}$$

where

$$\omega_s = -\sqrt{\frac{\eta q\dot{V}_{\mathrm{rf}}(0)}{E_oT_o}} \qquad \alpha = \frac{D}{2T_o}.$$

The vector

$$X = \begin{pmatrix}\phi \\ p\end{pmatrix}$$

is defined, so that Eq. (6) can be rewritten as

$$dX = AX(t)dt + dv,$$

where

$$A = \begin{bmatrix} 0 & 1 \\ -\omega_s^2 & -2\alpha \end{bmatrix} \qquad \frac{dv}{dt} = \begin{bmatrix} 0 \\ \omega_s^2 \end{bmatrix}\tilde{\phi}(t) = K\tilde{\phi}(t).$$

To estimate the bunch length σ_z, it is necessary to determine the second order moment of ϕ, since

$$\sigma_z = \frac{c}{\omega_{\mathrm{rf}}}\sigma_\phi.$$

Following the procedure outlined in [3,4], the autocorrelations of the perturbation $R_{\tilde{\phi}\,\tilde{\phi}}$ and output R_{xx}, as well as their cross correlation $R_{\tilde{\phi}x}$, are determined. It should be noted that $R_{\tilde{\phi}\,\tilde{\phi}}$ and $R_{\tilde{\phi}x}$ are wide sense stationary:

$$\begin{aligned}
R_{\tilde{\phi}\,\tilde{\phi}}(t_2 - t_1) &= E[\tilde{\phi}(t_2)\tilde{\phi}(t_1)] = \left[\left(\textstyle\sum_{k=-\infty}^{\infty}\delta(t_2 - kT_o)h_g(t_2)\right) * E[n_g(t_2)n_g(t_1)] * \left(\textstyle\sum_{k=-\infty}^{\infty}\delta(t_1 - kT_o)h_g(t_1)\right)\right] \\
R_{\tilde{\phi}x}(t_2 - t_1) &= \int_{-\infty}^{t_1} E[\tilde{\phi}(t_2)\tilde{\phi}(t_1 - \theta)]\left(e^{A\theta}\begin{bmatrix} 0 \\ \omega_s^2 \end{bmatrix}\right)^T d\theta = \int_{-\infty}^{t_1} R_{\tilde{\phi}\,\tilde{\phi}}(t_2 - t_1 + \theta)\left(e^{A\theta}\begin{bmatrix} 0 \\ \omega_s^2 \end{bmatrix}\right)^T d\theta \\
&= \int_{-\infty}^{t_1} R_{\tilde{\phi}\,\tilde{\phi}}(t_2 - t_1 - \theta)\left(e^{-A\theta}\begin{bmatrix} 0 \\ \omega_s^2 \end{bmatrix}\right)^T d\theta \\
R_{xx}(t_2, t_1) &= \begin{bmatrix} \sigma_\phi^2(t_2, t_1) & E[\phi(t_2)p(t_1)] \\ E[p(t_2)\phi(t_1)] & \sigma_p^2(t_2, t_1) \end{bmatrix} = \int_{-\infty}^{t_2} e^{A\theta}\begin{bmatrix} 0 \\ \omega_s^2 \end{bmatrix} E[\tilde{\phi}(t_2 - \theta)x^T(t_1)]d\theta \\
&= \int_{-\infty}^{t_2} e^{A\theta}\begin{bmatrix} 0 \\ \omega_s^2 \end{bmatrix} R_{\tilde{\phi}x}(t_2 - t_1 - \theta)d\theta,
\end{aligned} \tag{7}$$

where $E[x]$ denotes the expectation value of the random variable x, $e^{A\theta}$ is a matrix exponential, and A^T indicates the transpose of matrix A.

Since the system is linear and stable, the expressions in Eq. (7) converge to equilibrium values defined by the noise power and synchrotron radiation damping. These equilibrium values can be estimated by setting $\tau = t_2 - t_1$ and then taking the limit of Eq. (7) as t_1, $t_2 \to \infty$, since R_{xx} is asymptotically wide sense stationary, to get

$$R_{xx}(\tau) = e^{A\tau} * \begin{bmatrix} 0 & 0 \\ 0 & \omega_s^4 \end{bmatrix} R_{\tilde{\phi}\,\tilde{\phi}}(\tau) * e^{-A^T\tau} \tag{8}$$

which gives the correlation matrix due to the noise perturbation filtered by both the rf station and the beam dynamics. By applying the Fourier transform to $R_{xx}(\tau)$ from Eq. (8) and substituting for the noise autocorrelation $R_{\tilde{\phi}\,\tilde{\phi}}(\tau)$ from Eq. (7), the power spectral density $S_g(f)$ of $X(t)$ due to the generic term is obtained:

$$S_g(f) = B_g S_{N_g}(f) B_g^H, \tag{9}$$

where the superscript H denotes transpose complex conjugate, $S_{N_g}(f) = \mathcal{F}\{E[n_g(t_1)n_g(t_2)]\}$, and B_g is given by

$$\begin{aligned}
B_g &= (2\pi i f I - A)^{-1}\begin{bmatrix} 0 & 0 \\ 0 & \omega_s^2 \end{bmatrix}\left(\sum_{k=-\infty}^{\infty}\delta(f - kf_{\mathrm{rev}})\right) \\
&\quad * H_g(f) \\
&= (2\pi i f I - A)^{-1}\begin{bmatrix} 0 & 0 \\ 0 & \omega_s^2 \end{bmatrix}\sum_{k=-\infty}^{\infty} H_g(f - kf_{\mathrm{rev}}),
\end{aligned}$$

where f_{rev} is the beam's revolution frequency, $H_g(f) = \mathcal{F}[h_g(t)]$ is the frequency response of the rf station for a particular source and channel, and $(2\pi i f I - A)^{-1}$ is a matrix transfer function characterizing the beam filtering of the noise spectrum.

Extending the analysis to all noise sources and channels, the total spectral density $S_x(f)$ is given by

$$S_x(f) = \sum_m [B_i^m S_{N_i}^m(f)(B_i^m)^H + B_q^m S_{N_q}^m(f)(B_q^m)^H]. \tag{10}$$

Then, the square of the equilibrium bunch length σ_z^2 is given by

$$\sigma_z^2 = \frac{c^2}{\omega_{\mathrm{rf}}^2}\sigma_\phi^2 = 2\frac{c^2}{\omega_{\mathrm{rf}}^2}\begin{bmatrix} 1 & 0 \\ 0 & 0 \end{bmatrix}\int_0^\infty S_x(f)df \tag{11}$$

since the autocorrelation $R_{xx}(\tau)$ is an even function.

It is obvious from Eqs. (10) and (11) that the bunch length depends on the noise power spectrum injected, filtered by the corresponding rf station and beam transfer functions as intuitively expected. The aliasing effect of the periodic sampling of the accelerating voltage signal can also be seen. This aliasing effect practically folds the bandwidth of the closed loop rf station response (≈ 300 kHz) on the band between DC and $f_{\mathrm{rev}} = 11.245$ kHz. The aliasing greatly enhances the effect of the noise on the beam dynamics and multiplies the noise power spectrum by almost a factor of 30. From this analysis it also follows that the aliased and loop shaped noise power spectral density at the synchrotron frequency f_s is critical for the determination of the equilibrium bunch length, as seen from the beam transfer function depicted

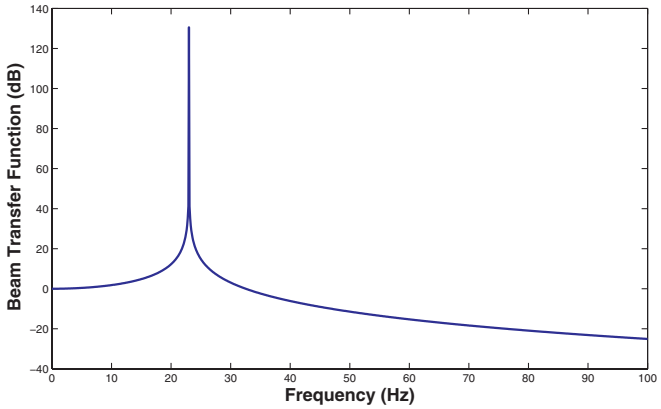

FIG. 3. (Color) Beam transfer function during physics defined by $[1\ 0](2\pi ifI - A)^{-1}[0\ \omega_s^2]^T$. As expected, the resonance is at the synchrotron frequency of about 22 Hz for the physics configuration. The resonance is even sharper during injection due to the longer synchrotron radiation damping time.

in Fig. 3, which shows the relationship between the beam phase and the sampled cavity phase.

It should be noted that with this treatment, the individual noise sources with power spectrum density $S_N(f)$ can be shaped or colored noise sources. This is an advantage of this formalism over a similar analysis using the Fokker-Planck equation, which cannot be extended to colored noise sources, or to white noise sources shaped by the dynamics of the rf station, as discussed in [5,6].

In this treatment we considered a single rf station. It is obvious from this result that the equilibrium bunch length will depend on the total power sampled by the beam. By superposition, this will be equal to the sum of the power introduced to the beam from all the rf stations.

IV. AN APPLICATION TO SINGLE-BUNCH DYNAMICS

Because of the very low synchrotron radiation of the protons in the LHC and the use of klystrons as final amplifiers in the rf stations, the LHC longitudinal beam emittance greatly depends on rf station perturbations and noise. Earlier studies [7] have determined the substantial variation of the LHC bunch length, but have considered the rf system as a generator in steady state. In this work, rf dynamics are now included, as well as the aliasing effect of the beam's periodic sampling of the cavity voltage on the noise power spectrum.

The equilibrium value of the bunch length can be calculated by evaluating the integral of $S_x(f)$ as shown in Eq. (11), by establishing the transfer function $H_g(f)$ for a given operation point, and using the known linearized beam dynamics defined by matrix A and the injected noise power spectral density S_{N_g}.

Since it is impossible to separate the contributions to the total cavity noise from the various noise sources and channels, noise is only injected in one point at a time during the simulations. For a given transfer function $H_g(f)$ it is then possible to determine the noise power spectral density S_{N_g} that will achieve $\sigma_\phi(\infty) = \sigma_\phi(0)$, thus keeping the initial beam distribution during a store. These values are a useful metric of the total power injected to the beam for each channel and noise source. Thus, they are significant of the relative importance of all the sources. This is very helpful for the analysis of the system performance, since all of the major noise sources can be modeled by an equivalent white noise source in the bandwidth of the rf loop.

As a result, different operation points provide different noise levels at the accelerating voltage. The changes of the rf station phase noise floor level due to different settings of the LLRF feedback loops are studied, to determine the sensitivity of the longitudinal beam emittance on various rf parameters. With these results it should be possible to determine in the future what technical components dominate the noise level and how changes in digital quantizing choices and analog components impact the emittance growth.

A. Transfer function estimation: Time-domain simulation

To determine the transfer function between the noise sources and the phase of the rf accelerating voltage, a time-domain simulation of the LHC rf station-particle beam interaction is used [8]. The time-domain simulation allows a simple representation of analog and digital components, as well as the inclusion of nonlinear elements. By linearizing around each operation point, it is possible to determine the frequency domain transfer function. The close relationship between the LHC and PEP-II rf systems allows the use of previous experience and tools from PEP-II operations on the LHC studies [9,10]. Detailed descriptions of the systems have been presented for PEP-II [9] and LHC [11].

The simulation captures the architecture, parameters, technical implementation, nonlinearities, and engineering details of the LLRF and rf systems. Noise effects, quantizing effects in digital systems, and dynamic range effects could also be introduced. All components shown in Fig. 1 are included in the simulation. Because of the computation complexity, it is only reasonable to run the simulation for the equivalent of tens of milliseconds of real machine time. It is then possible to extract beam and station parameters to study the longitudinal beam dynamics and the rf station operation. The time-domain simulation has also been used as a development environment for the LHC optimization and configuration tools [12,13].

B. rf station configurations of interest

Each operation point is defined by the rf station configuration; the set of values for all the adjustable loop parameters. These parameters are (1) beam parameters, such as the

beam energy and average beam current, (2) high-level rf station settings: the klystron operation point, the cavity voltage, detuning, and loaded quality factor Q_L, and (3) the LLRF parameters, analog/digital loop gain G, controller phase ϕ, and 1-Turn feedback gain and delay. The choices of values for this work is described below.

For each operation point, the beam and high-level rf parameters are predetermined. Based on these operational conditions and the current technical implementation of the LHC rf system, the LLRF parameters are then adjusted to reduce the cavity fundamental impedance presented to the beam, while satisfying rf loop stability requirements. The optimal values are determined for each configuration, using the same LHC optimal configuration tools as in the real system [12–14].

1. Beam parameters

During normal operations, each of the LHC's rings is filled from the Super Proton Synchrotron with particles at an energy of 450 GeV and then ramped to the collision energy (nominally 7 TeV per beam). There are three interesting stages of the LHC operation: at the beginning of injection ($I_o = 0$ A), at the end of injection with maximum current at low energy, and the physics/collision phase at higher energy. The beam and rf station dynamics change considerably during these steps.

At the nominal current of 0.58 A, the LHC klystrons will be operating at approximately 297 kW close to the maximum value of 330 kW. Therefore, the LHC klystrons are operated close to saturation. In order to separate possible saturation effects in this work, studies are conducted at both the nominal current of 0.58 A DC and at the more conservative value of 0.3 A DC.

2. High-level rf settings

For the studies presented in this paper, the cavity voltage V_c and loaded quality factor Q_L are set to 1 MV and 20 000, respectively, during injection and to 2 MV and 60 000 during the physics phase.

The LHC beam current is irregular around the ring due to the bunch pattern and the voltage is kept constant over the turn thanks to the rf and 1-Turn feedback systems. If the cavity were to be detuned for minimum klystron power with the beam present, then the klystron would have to switch between two power levels in the presence and absence of beam. To minimize klystron power over one turn, the cavity is set using the half-detuning algorithm during LHC operation [14–16]. The half-detuning algorithm decreases the instantaneous power of the klystron in the absence of beam and keeps the klystron power constant during the changes in the beam pattern. The same scheme is used in the simulations presented in this work.

3. LLRF parameters

The LLRF parameters adjusted during this work are the feedback gain, the 1-Turn delay, and the loop phase. The 1-Turn feedback loop gain and phase are not adjusted during operations, but are set to 20 dB and 0°, respectively.

Table I shows the cavity detuning f_d and the LLRF parameters for each operational scenario considered, as described above. It should be noted that G and ϕ are reference values that define relative changes to the parameters set in the hardware. Using the simulation, a 9 dB gain margin was estimated for the 1-Turn feedback loop, close to the 10 dB value reported during development [17]. The 1-Turn feedback loop delay τ_d is optimized during operations. For the simulation the optimal value was 87.8 μs. As expected, the LLRF configuration changes significantly during the LHC ramp, whereas during injection the LLRF parameters are essentially unchanged (low beam loading), and only the klystron forward power shows a noticeable effect.

The LHC optimal configuration tools inject noise to the rf station for a brief period of time to characterize the rf station through a transfer function measurement. Because of beam emittance blowup concerns, the optimal configuration tools will not be used in the presence of beam according to the current operational plan. As a result, with the current operation plan the LLRF is optimized with no beam before injection, and then the LLRF is kept at the same settings throughout the LHC operation, thus significantly reducing the performance of the rf station compared to a situation where the parameters are adjusted at each stage. To estimate the effect of this operational scenario, the simulation is run using the optimal LLRF parameters calculated at $I_o = 0$ but at the physics configuration with $I_o = 0.3$ A. The results are reported under

TABLE I. rf and LLRF parameters for beginning/end of injection and physics-collision configurations considered in this paper.

	Beam		High-level rf			LLRF	
Configuration	I_o (A)	V_c (MV)	Q_L	P_{kl} (kW)	f_d (kHz)	G (dB)	ϕ
Injection beginning	0	1	2×10^4	139	0	17.44	24°
Injection end	0.3	1	2×10^4	149	−2.7	17.44	2.4°
Physics	0.3	2	6×10^4	216	−1.35	22.35	5°
Injection end	0.58	1	2×10^4	177	−5.3	17.82	2.6
Physics	0.58	2	6×10^4	298	−2.65	23.3	8°

TABLE II. Modulator and LLRF noise threshold in $\mathrm{nV}/\sqrt{\mathrm{Hz}}$ for injection configurations. These values correspond to the rf settings shown in Table I.

Configuration	$V_{\mathrm{modulator}}$ i	q	V_{LLRF} i	q
Injection beginning	7.3×10^{-2}	7.9×10^{-3}	3.3×10^{-2}	1.3×10^{-3}
Injection end 0.58 A	8.3×10^{-2}	8.4×10^{-3}	9.2×10^{-3}	1.2×10^{-3}
Injection end 0.3 A	9.8×10^{-2}	8.0×10^{-3}	1.7×10^{-2}	1.3×10^{-3}
Nonoptimal injection end 0.3 A	3.3×10^{-2}	6.4×10^{-3}	2.1×10^{-3}	5.7×10^{-4}

TABLE III. Modulator and LLRF noise threshold in $n\mathrm{V}/\sqrt{\mathrm{Hz}}$ for physics configurations. These values correspond to the rf settings shown in Table I.

Configuration	$V_{\mathrm{modulator}}$ i	q	V_{LLRF} i	q
Physics 0.58 A	1.1×10^{3}	270	30	18
Physics 0.3 A	2.4×10^{3}	180	120	18
Nonoptimal physics 0.3 A	2.1×10^{3}	210	360	29

''Nonoptimal physics'' in Table III. In a hypothetical scenario, it would be possible to estimate the optimal LLRF parameters for physics/collision using the simulation, and then use those settings during injection, ramping, and physics. This scenario will have reduced performance at injection, and the corresponding results are reported as ''Nonoptimal injection end'' in Table II.

C. Results

To determine the noise power threshold at the output of the LLRF and the modulator, the simulation is set to the configurations of interest and the transfer function $H_g(f)$ between the noise (i or q) and the phase of the cavity voltage is measured. As described in Eq. (1), the transfer functions for all sources and channels should be measured for each operational condition. The transfer function between the rf accelerating voltage phase and the noise at the q channel at the input of the modulator is shown in Fig. 4 as an example. Assuming a wideband noise source of power constant spectral density $(N^m)^2$ for source m, Eq. (11) can be simplified to

$$\sigma_z^2 = \frac{2c^2}{\omega_{\mathrm{rf}}^2}(N^m)^2 \int_0^\infty B^m (B^m)^H df. \tag{12}$$

Then, it is possible to estimate the ratio between the phase modulation in the rf accelerating voltage and the noise source for each of the configurations. This ratio is calculated using the transfer function from the whole band which is aliased over the frequency band from the rf operating frequency out to the first revolution harmonic following Eqs. (9)–(11).

The power spectral density N_o^2 for one channel in a single rf station that achieves an equilibrium bunch length equal to the initial condition for source m, can be calculated using this information, so that it is possible to calculate the noise spectral density for each source that achieves that bunch length:

$$N_o^2 = \frac{\sigma_{z_o}^2 \omega_{\mathrm{rf}}^2}{2c^2 \int_0^\infty B^m (B^m)^H df}$$

for σ_{z_o} equal to 11.24 and 7.55 cm during injection and physics, respectively. The results of these calculations for all the configurations of interest are shown in Tables II and III for injection and physics configurations, respectively. As expected, the noise threshold is significantly lower for the injection configurations, since the synchrotron radiation damping is more than 3 orders of magnitude lower. The very low thresholds for the injection configurations are not a reason for concern though, since the beam is kept in this condition for a short time. On the other hand, the large sensitivity on the synchrotron radiation and consequently on the beam energy levels implies that the planned low energy operation at 3.5 TeV will reduce the noise threshold limits. Furthermore, one can see the wide variation with rf configuration and input channel (i or q), as expected from the synchronous phase of $\approx 180°$. Table II shows the impact of the different configurations: the LLRF noise threshold is scaled by a factor of 2 when the LLRF is operated with the physics configuration during injection

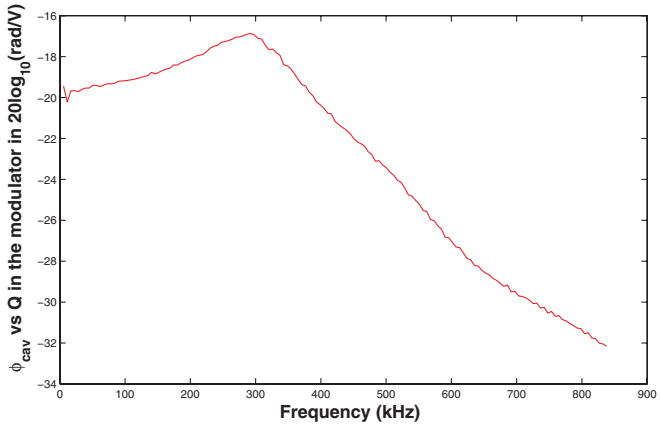

FIG. 4. (Color) The transfer function between the rf accelerating voltage phase and the noise at the q channel at the input of the modulator $\{[\phi_{\mathrm{cav}}(f)]/[n_q^{\mathrm{mod}}(f)]\}(\mathrm{rad}/V)$.

(the noise threshold decreases to 5.7×10^{-4} nV/$\sqrt{\text{Hz}}$ from the optimal 1.3×10^{-3} nV/$\sqrt{\text{Hz}}$). Using the nonoptimal configurations lowers the noise threshold as anticipated. On the other hand, in Table III there is a factor of 1.6 *increase* of the noise threshold when the LLRF is operated with the injection settings during physics (from 18 to 29 nV/$\sqrt{\text{Hz}}$). This small increase though results in a substantial cost to beam stability, since the LLRF gain—and consequently the fundamental impedance reduction—is now reduced by 5 dB.

As explained above, these results correspond to only one active noise source and channel at the time. They also represent only one of the eight stations per beam. Therefore, a scheme has to be devised to determine the final threshold. It is straightforward to show that the total power spectral density at the accelerating voltage phase is given by the sum over all channels and sources. Assuming uncorrelated wideband noise sources of varying constant spectral densities and using Eq. (1), Eq. (12) becomes

$$\sigma_z^2 = 8\frac{2c^2}{\omega_{\text{rf}}^2}\sum_m (N^m)^2 \int_0^\infty B^m (B^m)^H df$$
$$\frac{\sigma_z^2}{\sigma_{z_o}^2} = 8\sum_m \frac{(N^m)^2}{(N_o^m)^2}. \tag{13}$$

Therefore, the values presented in Tables II and III provide the weighting coefficients for the contributions of the individual noise sources to the equilibrium bunch length. As such, the noise contributions are dominated by the source with the lower threshold or with a significantly higher noise power.

Equation (13) can be very helpful for the system designer, since the values N^m can be set based on the technical challenges related to reducing the noise levels of each source. These noise levels define the design specifications for the LLRF and modulator boards and can be compared with the expected noise levels of the architecture. Dedicated measurements will be necessary to compare

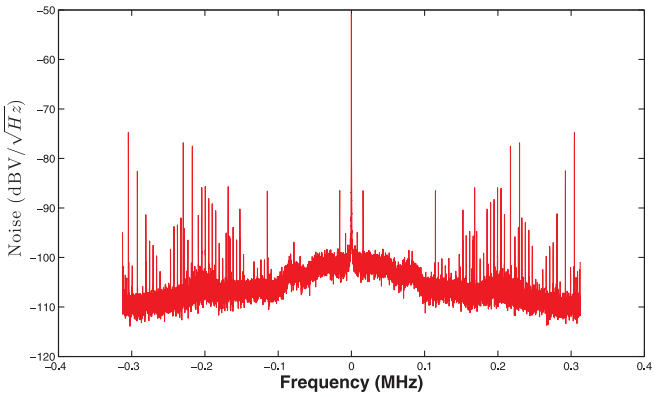

FIG. 5. (Color) Noise power spectral density at the output of the LHC rf feedback for channel Q (wideband).

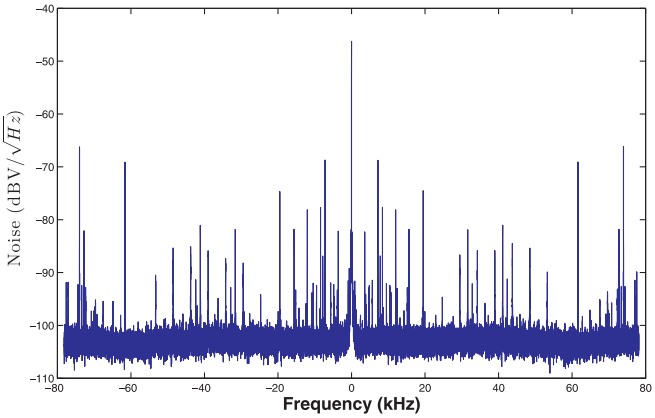

FIG. 6. (Color) Noise power spectral density at the output of the LHC rf feedback for channel Q (narrow band).

with the noise of the actual implementation and verify the calibration of the simulation signals.

Some initial measurements of the noise spectrum at the output of the LHC LLRF feedback board are shown in Figs. 5 (wideband) and 6 (narrow band). These measurements were conducted with the LLRF feedback board input terminated to 50Ω. These noise levels should be comparable to the levels at the input of the modulator. The value of approximately 7 μV/$\sqrt{\text{Hz}}$ in the bandwidth of the accelerating cavity is higher than the thresholds in Table III, so a slow growth of longitudinal emittance is anticipated. Ongoing work will test the validity of this prediction.

V. MULTIBUNCH STABILITY

Various studies have been conducted to evaluate the longitudinal coupled-bunch instabilities at the LHC [18,19]. These studies do not include the cavity fundamental impedance nor consider the effect of the LLRF impedance reduction feedback system though. Using the time-domain simulation and related models presented in Sec. IV, it is possible to estimate the effective impedance presented to the beam by the rf station for any configuration. The coupled-bunch instabilities can then be computed to study the bunch centroid stability, position, and motion due to multibunch coupling as a function of the rf configurations.

An advantage of the time-domain simulation approach is the ability to vary individual LLRF feedback parameters and determine their effect on the beam stability. As a result, the sensitivity on individual rf parameters can be estimated, and the possible tradeoffs between beam and rf station stability can be investigated. The related results are presented in Sec. V B.

Impedance reduction is of fundamental importance at the LHC since there is no dedicated bunch-by-bunch longitudinal feedback system. The substantial bunch length leads to stability through Landau damping. The effective cavity impedance though depends strongly on the LLRF configurations. In this section, the coupled-bunch instabil-

ities are investigated as a function of the LLRF configurations to determine the stability margins for the LHC.

The effective cavity impedance is computed using a linearized model of the rf station and LLRF feedback around the operation point [20], based on the system operating points determined from the nonlinear simulation tools. For operation with $V_{\mathrm{cav}} = 2$ MV and $Q = 60$ k, the analog/digital loop and the 1-Turn feedback provide a reduction of the superconducting cavity impedance of about 50 dB around mode 0, as expected.

Using the estimated impedance and assuming a Gaussian bunch, the growth rate σ_l and tune shift $\Delta\omega_l$ can be computed for each coupled-bunch mode l [21]:

$$\sigma_l + j\Delta\omega_l = \frac{\eta q I_o}{2\beta^2 \omega_s E_o T_o} \sum_{p=-\infty}^{\infty} Z(\omega)\omega e^{\sigma_\tau^2 \omega^2}, \qquad (14)$$

where η is the slip factor, q is the charge of a proton, I_o is the DC beam current, β is the ratio of the particle speed to the speed of light, ω_s is the synchrotron frequency, E_o is the beam energy, T_o is the revolution period, Z is the estimated rf station impedance contributed from all eight stations per beam, and σ_τ the bunch length in time units. The impedance is evaluated at frequencies $\omega = (ph + l)\omega_o + \omega_s$ with ω_o the angular revolution frequency, h the harmonic number, l the mode number, and p any integer. Figures 7 and 8 show an example of the resulting modal growth rates and tune shifts for configuration injection end 0.3 A with the 1-Turn feedback on or off. The reduction of the growth rates and tune shifts for all lower order modes—except for mode 0—is evident.

A. Stability criterion

The interaction between the cavity fundamental impedance and the beam produces growth rates in the order of seconds when the LLRF feedback system is operating. Even though these growth rates are very slow—tens of thousands of turns—they are critical, because the synchrotron damping time is in the order of hours (approximately 50 000 and 13 hours for injection and physics, respectively). Since there is no bunch-by-bunch feedback system, stability is determined by Landau damping—a physical process which stabilizes the otherwise unstable ensemble of oscillating particles due to a spread of their natural frequencies caused by the nonlinearity of the rf voltage. To determine stability, the criterion defined in [22–24] is used with the same safety margins:

$$\sigma_l < \frac{\Delta\omega_s}{4},$$

where $\Delta\omega_s$ is the synchrotron frequency spread within the bunch. The synchrotron frequency spread is given by

$$\Delta\omega_s = \omega_s \frac{\pi^2}{16}\left(\frac{hL}{2\pi R}\right)^2,$$

where $h = 35\,640$ is the harmonic number, L is the total bunch length ($4\sigma_z$), and $R = 4242.893$ m is the LHC radius. Since the LHC rms bunch length is 11.24 and 7.55 cm during injection and collision, respectively, $\Delta\omega_s/4$ is equal to 1.19 and 1.55 for these two cases.

The growth rate of the most unstable mode $\sigma_{\max}$ and the maximum tune shift $\Delta f_{\max}$ for each configuration are

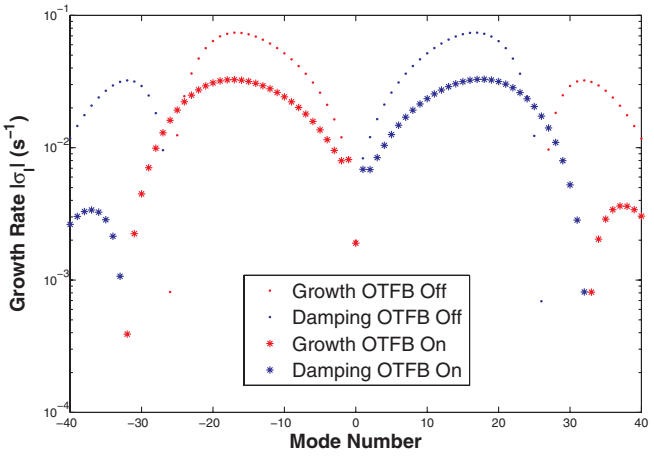

FIG. 7. (Color) Modal growth rates for configuration injection end 0.3 A with 1-Turn feedback (OTFB) on or off.

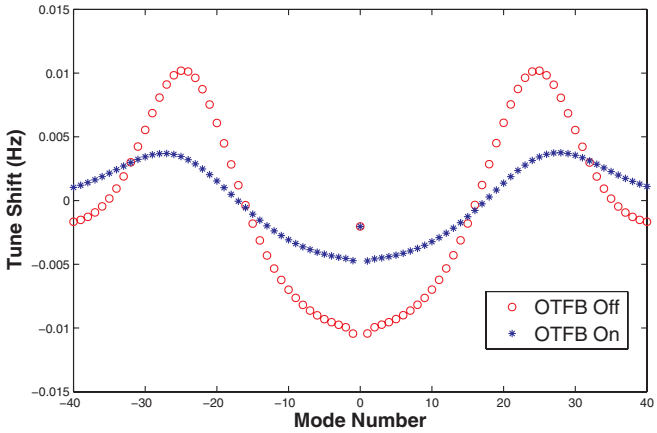

FIG. 8. (Color) Tune shift for configuration injection end 0.3 A with 1-Turn feedback (OTFB) on or off.

TABLE IV. Growth rates of the most unstable mode and maximum tune shifts for each configuration, with the 1-Turn feedback on.

Configuration	$\sigma_{\max}$ (s^{-1})	$\Delta f_{\max}$ (Hz)
Injection end 0.58 A	0.055	0.0071
Physics 0.58 A	0.0041	0.0011
Injection end 0.3 A	0.033	0.0047
Physics 0.3 A	0.0061	0.0009
Nonoptimal injection end 0.58 A	0.083	0.0099
Nonoptimal physics 0.3 A	0.019	0.0044

reported in Table IV. Comparing the results from Table IV with the threshold margins of 1.19 and 1.55 for injection and physics, the fastest growth rate is at least a factor of 20 smaller than the stability criterion threshold for all configurations. It is also obvious that the configurations at physics have lower growth rates than those at the end of injection due to the almost twentyfold increase in beam energy. It should be mentioned that the estimated impedance driven tune shifts are insignificant compared to the frequency spread due to the nonlinearity of the rf voltage.

It is important to note the significant effect that changes of the LLRF configuration can have on the modal growth rates, as can be seen for the almost threefold increase in growth rates with the nonoptimal configurations. Even though the stability threshold is not crossed, it is important to notice the importance of the optimal LLRF tuning not only for the rf station stability, but also for beam stability. The tuning can be even more critical for lower beam energies. As seen from Eq. (14), the growth rates are inversely proportional to the beam energy E_o. During the initial LHC runs, the beam energy has been and will be kept at much lower levels than the nominal 7 TeV. To maintain the margin level calculated above, the current I_o should be scaled similarly. For example, an LHC configuration with the nominal current of 0.58 A at an energy of 1 TeV will cause coupled-bunch instabilities with growth rates 7 times higher than those presented in Table IV, and would probably lead to beam loss. Once again, operation at lower energies can have negative effects on the longitudinal beam dynamics.

B. Growth rate sensitivity to LLRF parameters

One of the important features of the LHC time-domain simulation is the ability to study alternative configurations of the rf and LLRF system, without requiring time from the real machine. As such, it can be used to analyze the sensitivity of the modal growth rates to variations of the LLRF parameters. These studies provide insight on the limits of the implementation, on the operational margins, and on the parameters most essential to reliable operations.

Using the configuration at the end of injection with a beam current of 0.3 A as a reference, each of the following parameters were modified separately to understand their impact in the interaction between the rf station and the beam dynamics: Cavity detuning f_d, analog/digital loop gain G, controller phase ϕ, and 1-Turn feedback loop gain G_c and phase ϕ_c. The variations on each case were determined to correspond to reasonable variations over a run. The system's impedance and corresponding growth rates were estimated for each case. The growth rates of the fastest growing mode for each case are reported in Table V. It is interesting to see the considerable beam stability dependence on the controller phase and the 1-Turn feedback phase. A sixfold increase of the growth rates with a controller phase rotation of 10° reduces the margin of operation to a factor of 3, which then limits the maximum reliable current for energy levels lower than 7 TeV. This analysis shows the critical importance of careful tuning of the LLRF in cases where the beam stability margin is limited.

TABLE V. Growth rate sensitivity on LLRF parameters.

Parameter Nominal Value	Adjustment	Growth rate 0.033	Change
f_d	±1 kHz	0.038/0.028	+15/ − 15%
G	±3 dB	0.028/0.043	−16/ + 31%
ϕ	±10°	0.23/0.19	**+590**/ + **490**%
G_c	±3 dB	0.026/0.039	−20/ + 20%
ϕ_c	±10°	0.12/0.10	+270/ + 220%

It is not surprising that there are changes in LLRF parameters that improve beam stability. The LLRF is tuned in a manner that maximizes the stability of both the beam and the rf-LLRF loop. For example, the cavity detuning f_d is set to minimize the average klystron power. The analog/digital loop gain as well as the 1-Turn feedback loop gain are set to achieve predetermined gain margins. Therefore, a tradeoff exists between beam and loop stability.

A similar study was performed for variations of the 1-Turn feedback delay. The total delay in the 1-Turn feedback loop is set by a coarse delay of 100 ns increments, and a fine delay of 10 ps increments. In our study, no considerable effects on the estimated growth rates were experienced even when the delay was changed by a few hundred nanoseconds (corresponding to multiple taps of the coarse setting). On the other hand, a shift of even a few tens of nanoseconds is sufficient to bring rf station instability. Thus, optimal tuning of the 1-Turn feedback delay might not be critical for beam stability directly, but it is essential for rf station stability, and consequently for reliable operation with beam.

VI. CONCLUSIONS

A theoretical formalism for the study of rf noise effects on longitudinal beam emittance has been developed and is presented in this work. With this formalism and the LHC rf and LLRF models and simulation [8], the effect of rf and LLRF configurations on the longitudinal beam emittance growth has been estimated. Noise threshold limits for the input of the modulator and the LLRF have been explored. These results can be helpful for noise allocation and specification of technical components in future designs.

The LHC rf and LLRF models and simulation are valuable tools in the study of the rf station/beam dynamics interaction, and have been used in this work to also study multibunch stability. The variations of stability margins with operational choices and the system sensitivity on individual controller settings have been presented.

Dedicated measurements at the real system are planned to determine the noise levels with the installed architecture

and compare the expected and actual beam emittance growth as a function of the rf noise and configuration. With the simulation and models any other possible configuration, proposed design, algorithm, or next generation system can be studied.

ACKNOWLEDGMENTS

The authors would like to thank the CERN BE-RF group for their help, support, and interest in all phases of this project. Conversations with Alex Chao and Ron Ruth at SLAC were very helpful for the development of the single-bunch longitudinal beam emittance growth formalism. The authors are also grateful to Joachim Tuckmantel at CERN for all his inspiring work on the longitudinal beam blowup effects. Alex Bullitt at SLAC contributed to the clarity and organization of this article. The US-LARP program and SLAC AARD group have greatly supported this work. This work was supported by the DOE through the U.S. LHC Accelerator Research Program (LARP) and under Contract No. DE-AC02-76SF00515.

[1] J. Tuckmantel, LHC Project Note-404, 2007.
[2] M. Sands, Report No. SLAC-PUB-0121, 1970.
[3] K. Astrom, *Introduction to Stochastic Control Theory* (Dover Publications, Mineola, NY, 1970), pp. 63–66.
[4] H. Stark and J. Woods, *Probability, Random Processes, and Estimation Theory for Engineers* (Prentice Hall, Englewood Cliffs, NJ, 1994), p. 401–407, 437–442.
[5] Th. Leiber *et al.*, Phys. Rev. Lett. **59**, 1381 (1987).
[6] A. Burov, V. Lebedev, and Y. Alexahin (private communication).
[7] J. Tuckmantel, LHC Project Report No. 819, 2005.
[8] T. Mastorides *et al.*, in *Proceedings of the 11th European Particle Accelerator Conference, Genoa, 2008* (EPS-AG, Genoa, Italy, 2008).
[9] C. Rivetta *et al.*, Phys. Rev. ST Accel. Beams **10**, 022801 (2007); SLAC-PUB-12374, 2007.
[10] T. Mastorides *et al.*, Phys. Rev. ST Accel. Beams **11**, 062802 (2008); SLAC-PUB-13287.
[11] P. Baudrenghien *et al.*, in *Proceedings of the 10th European Particle Accelerator Conference, Edinburgh, Scotland, 2006* (EPS-AG, Edinburgh, Scotland, 2006).
[12] D. Van Winkle *et al.*, in *Proceedings of the 23rd Particle Accelerator Conference, Vancouver, Canada, 2009* (IEEE, Piscataway, NJ, 2009).
[13] D. Van Winkle *et al.*, in Proceedings of the 1st International Particle Accelerator Conference, Kyoto, Japan, 2010.
[14] P. Baudrenghien, Report No. CERN-AB-2007-011, 2007.
[15] D. Boussard, Reports No. CERN-SPS-ARF-DB-gw-Note-84-9 and No. CERN-LHC-NOTE-10, 1984.
[16] D. Boussard, in *Proceedings of the IEEE Particle Accelerator Conference, San Francisco, 1991* (APS Beam Physics, San Francisco, California, 1991).
[17] V. Rossi, Report No. CERN-BE-2009-009, 2009.
[18] D. Boussard *et al.*, LHC Project Note-205, 1999.
[19] E. Shaposhnikova, LHC Project Note 242, 2000.
[20] D. Teytelman, in *Proceedings of the 21st Particle Accelerator Conference, Knoxville, 2005* (IEEE, Piscataway, NJ, 2005).
[21] T. Suzuki, Y. H. Chin, and K. Satoh, Part. Accel. **13**, 179 (1983).
[22] A. Hofmann, CERN, Report No. 77-13, 1977, p. 139.
[23] F. Ruggiero, CERN Report No. SL/95-09 (AP), 1995.
[24] F. Sacherer, IEEE Trans. Nucl. Sci. **24**, 1393 (1977); CERN Report No. 77-13, p. 198, 1977.